Concurrent simulation of the eddying general circulation and tides in a global ocean model

Brian K. Arbic

Department of Oceanography and Center for Ocean-Atmospheric Prediction Studies,

Florida State University, Tallahassee, Florida, United States

Alan J. Wallcraft and E. Joseph Metzger

Oceanography Division, Naval Research Laboratory, Stennis Space Center, Mississippi,

United States

Corresponding author: Brian K. Arbic, Department of Oceanography and Center for Ocean-Atmospheric Prediction Studies, Florida State University, Tallahassee, Florida, 32306, United States

Email: barbic@fsu.edu

Submitted to *Ocean Modelling*

ABSTRACT

This paper presents a 5-year global simulation of HYCOM, the HYbrid Coordinate Ocean Model, that simultaneously resolves the eddying general circulation, barotropic tides, and baroclinic tides with 32 layers in the vertical and $1/12.5^{\circ}$ (equatorial) horizontal grid spacing. A parameterized topographic wave drag is inserted into the model and tuned so that the surface tidal elevations are of comparable accuracy to those in optimally tuned forward tide models used in previous studies. The model captures 93% of the open-ocean sea-surface height variance of the eight largest tidal constituents, as recorded by a standard set of 102 pelagic tide gauges spread around the World Ocean. In order to minimize the impact of the wave drag on non-tidal motions, the model utilizes a running 25-hour average to approximately separate tidal and non-tidal components of the bottom flow. In contrast to earlier high-resolution global baroclinic tide simulations, which utilized tidal forcing only, the run presented here has a horizontally non-uniform stratification, supported by the wind- and buoyancy forcing. The horizontally varying stratification affects the baroclinic tides in high latitudes to first order. The magnitude of the internal tide perturbations to sea surface elevation amplitude and phase around Hawai'i is quite similar to that seen in satellite altimeter data, although the exact locations of peaks and troughs in the model differ from those seen in the altimeter. Images of eddies and internal tides co-existing in the model are shown, and a discussion of planned future analyses that will extend far beyond the preliminary analyses shown here is given.

1 Introduction

This paper presents an early attempt to simultaneously resolve the oceanic general circulation, its associated mesoscale eddy field, and the barotropic and baroclinic tides, at high horizontal and vertical resolution, in a global model. We describe the numerical technique we have used to ensure an accurate barotropic tide without severely disrupting the mesoscale eddy field. As will be described below, it is far from trivial to ensure an accurate barotropic tide in forward global models, and the presence of non-tidal motions only increases the challenge. We present preliminary results from our simulation, including comparisons with satellite altimeter and tide gauge data. We present visual demonstrations of the co-existence of barotropic tides, baroclinic tides, and mesoscale eddies in the model. Finally, we briefly describe several detailed analyses we plan to undertake on this simulation in subsequent papers.

In recent years, several groups have simulated the global oceanic general circulation in numerical models with horizontal grids that are fine enough to resolve (or at least permit) mesoscale eddies, the transient turbulent features which contain a substantial fraction of the oceanic kinetic energy. For instance, the Parallel Ocean Program (POP) model has been run globally at $1/10°$ resolution (Maltrud and McClean 2005), the Naval Research Laboratory Layered Ocean Model (NLOM) is run in ocean forecast mode with $1/32°$ horizontal resolution (Shriver et al. 2007), the HYbrid Coordinate Ocean Model (HYCOM) is being developed as a $1/12.5°$ resolution forecast model (Chassignet et al. 2007), the Ocean General Circulation Model for the Earth Simulator (OfES) has been run at $1/10°$ resolution (Masumoto et al. 2004), and the Ocean Circulation and Climate Advanced Model (OCCAM) has achieved 1/12° horizontal resolution (Lee et al. 2007). At the same time, in recent years, high-resolution global models of the baroclinic tides have begun to be run (Arbic et al. 2004–hereafter, AGHS; Simmons et al. 2004–hereafter, SHA; Hibiya et al. 2006; Simmons 2008). In coastal models, it is common to model tides and non-tidal motions simultaneously. However, tides and non-tidal motions have almost always been simulated separately in global models. A few recent global simulations have been have included tides and non-tidal motions simultaneously (Schiller and Fiedler 2007; T. Dobslaw, M. Müller and M. Thomas, personal communication 2008), but these studies are done with model horizontal grid spacings of order one degree, at which neither mesoscale eddies nor baroclinic tides are resolved.[1] Here we merge two previously separate recent threads in the literature–high resolution modelling of the global general circulation, and high-resolution modelling of the global tides.

By combining these two threads we potentially improve the modelling of both types of motions, which affect each other in various ways. Interactions between mesoscale eddies and internal tides have the potential to transfer part of the coherent internal tide energy into incoherent signals, and to affect tidal energy budgets (Park and Watts 2006, Rainville and Pinkel 2006, Zaron et al. 2009, Chavanne et al. 2009a, 2009b). Park and Watts (2006) and Chavanne et al. (2009b) show that the variations in stratification induced by mesoscale eddies, in addition to the scattering arising from eddy velocities, have important effects on internal tide propagation. A mixed tidal/non-tidal model is also more likely to properly

[1] To be more precise, in Schiller and Fiedler 2007 the resolution was high in an area around Australia, but the telescoping grid they used led to low resolutions over most of the global ocean. The Dobslaw, Müller, and Thomas simulations are done for climate purposes and thus are run for much longer time periods than the runs discussed here, at much lower spatial resolution.

account for the effects of the quadratic bottom boundary layer drag term. Currently, many ocean general circulation models insert an assumed tidal background flow, typically taken to be about 5 cm s^{-1}, into the quadratic drag formulation (e.g., Willebrand et al. 2001). However, in the actual ocean tidal velocities vary from $\sim$ 1-2 cm s^{-1} in the abyss, to $\sim$ 0.5-1 m s^{-1} in areas of large coastal tides. Thus an assumed tidal background flow of 5 cm s^{-1} is too strong in the abyss, and too weak in coastal areas. By actually resolving the (spatially inhomogeneous) tidal flows in a general circulation model, we take a step towards correcting this problem. The explicit resolution of tides may represent an important step towards more realistic representation of mixing in high-resolution models, and we are currently pursuing this avenue as well. Finally, the stratification in a mixed tidal/non-tidal model can vary horizontally, since the wind- and buoyancy-forcing which supports this varying stratification is present. In contrast, the stratification in the earlier high-resolution global baroclinic tide simulations of AGHS and SHA was chosen to be horizontally uniform since these simulations did not include wind- and buoyancy-forcing. In both of these papers the stratification was taken from typical vertical profiles in subtropical areas, which cover large areas of the world ocean. However, these stratifications are very different from those in polar regions, and as a result the internal wave activity in the polar regions of these simulations was almost certainly unrealistically large (Padman et al. 2006). By embedding baroclinic tides in a horizontally varying stratification supported by realistic wind and buoyancy forcing, we can rectify these deficiencies.

The results presented here represent an important first step towards one of our long-term goals, to simultaneously resolve tides and non-tidal motions in global data-assimilative models with 1/25° horizontal resolution. Because the goal is an operational model, accuracy of all the resolved motions is paramount. We therefore desire to begin with forward models that are as accurate as possible. In recent years, it has been shown that achieving accurate surface elevations in forward global barotropic tide models requires the insertion of a parameterization of drag (and energy loss) due to the breaking of internal waves generated by tidal flow over rough topography (Jayne and St. Laurent 2001; Carrere and Lyard 2003; Egbert et al. 2004; AGHS; Lyard et al. 2006; Uehara et al. 2006; Griffiths and Peltier 2008, 2009). These parameterizations are motivated by inferences from tide models constrained by satellite altimetry of the dissipation of tidal energy in mid-ocean areas of rough topography (Egbert and Ray 2000), as well as in-situ evidence of elevated dissipation levels in such areas (e.g. Polzin et al. 1997). The subtleties of applying a parameterized topographic wave drag in models which resolve the generation of baroclinic tides, and in models which resolve non-tidal as well as tidal motions, will be discussed in the next section. A comparison and discussion of the accuracies of the barotropic tides in the baroclinic simulations of AGHS and SHA will prove to be instructive with regard to handling topographic wave drag in the new HYCOM simulations.

2 Inclusion of parameterized topographic wave drag

2.1 Need for parameterized wave drag in baroclinic tide models

In barotropic tide models, none of the internal waves generated by flow over rough topography are resolved, and all of this wave activity must be parameterized. In baroclinic tide models, the situation is more complicated and interesting. The resolved generation of low-mode internal tides means that the barotropic tide will be losing energy to the baroclinic tide in baroclinic models. Indeed, the computation of this energy conversion was a central goal of SHA, which built upon the baroclinic tide simulations performed for AGHS. Both studies were done with HIM, the Hallberg Isopycnal Model (Hallberg and Rhines 1996). Since in baroclinic tide models energy is lost from the barotropic mode, it is tempting to view parameterized topographic wave drag as redundant. Indeed, the main baroclinic simulation of SHA did not retain the parameterized topographic wave drag used in the main AGHS baroclinic simulations. We now examine the consequences of these different choices made in AGHS and SHA.

Table 1 shows the globally integrated available potential energy (APE) at the sea surface, and the globally integrated barotropic kinetic energy (KE; computed via standard formulae, which can be looked up in for instance AGHS), in 1) the satellite-constrained barotropic solutions of Egbert and Ray (2003), 2) the main baroclinic simulation of AGHS (see their Figure 11), which utilized topographic wave drag optimally tuned to minimize sea surface elevation errors with respect to satellite altimetry, 3) a baroclinic simulation of AGHS which did not utilize topographic wave drag and which also used only the scalar approximation (e.g., Ray 1998) for the self-attraction and loading term (in other words, run under conditions similar to the main baroclinic simulation of SHA), 4) the main baroclinic simulation of SHA, and 5) a baroclinic simulation of SHA briefly mentioned in their appendix, in which, inspired by Figure 2 of AGHS, an unrealistically large value of c_d (100 times the normal value) was utilized as a proxy for topographic wave drag. The globally- and temporally-averaged rms elevation errors of the forward models with respect to GOT99 (Ray 1999), a highly accurate altimetry-constrained tide model, are also shown. The errors are computed over waters deeper than 1000 m and over latitudes covered by the TOPEX/POSEIDON altimeter (equatorward of 66°).[2] Finally, the percentage of the GOT99 open-ocean sea surface height variance is shown. AGHS may be consulted for details of how the errors and percent variance captured are calculated. In the main baroclinic simulation of AGHS, the surface APE and barotropic KE are both quite close to the Egbert and Ray values, and as a result the surface elevation error is reasonably small. Note also that the barotropic energies and elevation errors in this optimally tuned AGHS baroclinic simulation are barely different from those in the optimally tuned one-layer simulation of AGHS (not shown). On the other hand, in the AGHS baroclinic simulation run without any parameterized topographic wave drag, the surface APE and barotropic KE are both about twice as large as the observed values. As a consequence the elevation discrepancy with respect to GOT99 is much larger, and the percentage of sea-surface height variance captured is much lower. Consistent with this result, both the potential and kinetic energies of the main SHA baroclinic simulation are also larger, by factors of about 3, than those in the accurate satellite-constrained models, and the high elevation error and low percent variance captured reflect this mismatch.[3] The large c_d simulation mentioned in the appendix of SHA performs much better with respect to the observations (and sees a factor of 2.4 drop in the conversion of barotropic to low-mode baroclinic energy), demonstrating that even artificial frictions can lead to accurate modeled

[2]To be precise, the errors in the SHA results were computed over the latitude range 66°S to 64°N, in order to avoid the complex tripolar grid utilized in the high latitudes of that study in the error computations.

[3]Consistent with the results of AGHS and SHA, a new simulation of baroclinic tides performed with ∼50 z-levels in the vertical direction and 1/4° horizontal resolution shows excessively large barotropic tides in the absence of parameterized topographic wave drag (Andrew Coward, Ariane Koch-Larrouy, Gurvan Medec, Adrian New, George Nurser, and David Smeed, personal communication 2009.)

tides as long as they remove energy at approximately the correct rate.

In the current study we have also found that the barotropic tide is extremely inaccurate if parameterized wave drag is not included. AGHS argued that a conversion of energy from barotropic to baroclinic tides in the models does not represent a loss of energy in the total (barotropic plus baroclinic) system, since the models do not resolve the breaking of baroclinic tides occuring in the actual ocean. Parameterized wave drag, unlike modal conversion, drains energy from the entire two-layer (two-mode) system. The bottom flow is a function of both barotropic and baroclinic tides, the latter contributing less when the stratification is surface-intensified, as is typical in the ocean. If we assume that wave breaking takes place mostly in the deep ocean, just above rough topography, and involves mostly high modes, then the parameterization represents the breaking of high modes near the bottom, which is not resolved in the baroclinic tide model. It remains to be seen whether this is the best representation of what actually happens in nature, but it is clearly true empirically that it results in far superior barotropic tides than those in simulations which do not utilize parameterized topographic wave drag. It is clear that any forward global tide model that aspires to be the backbone of an operational model must include a parameterized topographic wave drag, or perhaps some other way of removing energy from the model[4].

To end this subsection we note that despite the fact that the low-mode baroclinic tides have a weak signature at the bottom, it is evident that insertion of parameterized topographic wave drag into a baroclinic tide model affects the propagation distances of the low-mode internal tides. Contrast, for instance, the shorter propagation distances of the low-mode internal tide beams from their source regions shown in Figure 11 of AGHS with

[4]We are exploring the possiblity of removing energy directly from the resolved vertical shear.

the longer distances seen in Figure 8 of SHA.

2.2 Adaptation of parameterized wave drag used in previous studies

We utilize an adaptation of the topographic wave drag scheme described in the appendix of AGHS, which is based on the scheme outlined in Garner (2005). A multiplicative factor was included in the scheme and tuned to minimize the globally averaged deep-ocean rms elevation discrepancy between the forward model and GOT99. AGHS suggested that the multiplicative factor may compensate for the small scales that are absent in the roughness of present-day topographic datasets (e.g., Smith and Sandwell 1997). For the sake of simplicity, here we reduce the tensor scheme to a scalar scheme, utilizing energy considerations. We compute from 1/8° runs of the AGHS model the quantity

$$r = \frac{< \frac{d\vec{\mathbf{u}}_2}{dt}|_{topodrag} \cdot \vec{\mathbf{u}}_2 >}{< \vec{\mathbf{u}}_2 \cdot \vec{\mathbf{u}}_2 >}, \tag{1}$$

where angle brackets denote time-averaging and $\frac{d\vec{\mathbf{u}}_2}{dt}|_{topodrag}$ is the term in the momentum equation arising from the full tensor form of the topographic wave drag. Note that r is a linear drag coefficient, with $1/r$ as its e-folding time scale. We set the values of r to zero in regions shallower than 500 m and where it is small, i.e. where the e-folding time is greater than 30 days, which together account for 73% of the worlds ocean. This limits the impact of the wave drag on non-tidal motions (see next section). Finally, we clip the value of r so that its minumum e-folding time is 9 hours. Figure 1 shows maps of $1/r$ values obtained after all of these changes have been implemented. The drag is concentrated over well-known areas of rough topography such as the Mid-Atlantic Ridge, Southwest Indian Ridge, etc. In the $1/12.5°$ simulations we will be presenting shortly, we found that a multiplicative factor of 6 yielded accurate tides. Hence, the e-folding time of the applied drag is 1.5 hours to 6 days with no drag over 73% of the worlds oceans.

2.3 Utilizing topographic wave drag in the presence of non-tidal motions

On the relatively fast timescales of internal gravity waves, low-frequency motions such as mesoscale eddies and strong currents such as the Gulf Stream and Antarctic Circumpolar Current can be regarded as steady. The generation of internal gravity waves (lee waves) by steady flows over rough topography is a classic problem in geophysical fluid dynamics (e.g. Gill 1982). Tidal motions are oscillatory, not steady, and the work of Bell (1975) shows that the wave drag resulting from oscillatory flow over rough topography differs from the wave drag resulting from steady flow. In the future we may wish to include a parameterized wave drag for the non-tidal (steady, in this context) flow over rough topography in HYCOM. Indeed, some recent papers have argued that this mechanism represents a substantial energy loss for low-frequency motions (Naviera-Garabato et al. 2004, Marshall and Naviera-Garabato 2008, Nikurashin 2008). For now, however, we wish to have the wave drag acting only on the tidal part of the flow. This presents a challenge: how is the model to know the partition of tidal versus non-tidal bottom flows? In order to accomplish this separation, at least roughly, we utilize running 25-hour averages. The details of this scheme are discussed next.

2.4 Separation of tidal from non-tidal bottom flows

The topographic wave drag is nominally applied to the tidal flow only and acts on the bottom 500 m of the water column (recall that the drag is zero in waters shallower than 500 m). To filter out the tides we first form the average of 25 hourly samples of the velocity over the bottom 500 m lagged in time (i.e. from the previous 25 hours). This is the detided bottom flow $\overline{\vec{\mathbf{u}}_b}$ which is used as a correction to standard implicit linear friction over the bottom 500m of the water column:

$$\vec{\mathbf{u}}^{t+\Delta t} = \vec{\mathbf{u}}^{t-\Delta t} - 2\Delta t\sigma(\vec{\mathbf{u}}^{t+\Delta t} - \overline{\vec{\mathbf{u}}_b}) \tag{2}$$

Here, σ is the linear drag coefficient which in this case is $6r$. The friction is implicit for stability, given the large drag coefficient. A 25-hour average is not an exact tidal filter, and lagging it in time may introduce aliasing, but there are limits on what is practical in a running ocean model. In an 8-constituent tides only test case, adding the 25-hour filter had minimal effect on the accuracy of the tides. This issue is further explored in section 5.3.

3 Implementation of self-attraction and loading

Hendershott (1972) showed that global numerical tide models must account for self-gravitation of the ocean tide, solid earth deformation due to the load of the ocean tide, and perturbations to the gravitational potential due to the self-gravitation of the deformed solid earth. Collectively, these terms are known as the self-attraction and loading (SAL) term. A complete treatment of the SAL term requires computing a spherical harmonic decomposition of the ocean tide. This is not computationally feasible to do in the model as it runs, and instead is often done offline. An iterative procedure appears to be necessary to achieve numerical convergence (e.g., Egbert et al. 2004, AGHS). In the model runs presented here, as was done in SHA, we use the simpler scalar approximation, in which the SAL term η_{SAL} is approximated as a constant β times the sea surface elevation field η. In tides-only tests, we found that the optimal value of this constant in terms of minimizing the globally averaged rms sea surface elevation discrepancy with GOT99 is 0.06.

As pointed out by Hendershott (1972), the SAL term should apply to non-tidal as well as tidal flows. However, since SAL is not commonly applied to non-tidal flows, we choose to apply it only to the tidal component of sea surface elevations. Rather than using a lagged 25-hour average approach, as for bottom drag, we instead separate the sea surface elevation into steric and non-steric components and apply SAL only to the non-steric field.

4 Other details of the HYCOM simulation

HYCOM is a community ocean model (http://oceanmodeling.rsmas.miami.edu/hycom/) and uses a generalized (hybrid isopycnal/terrain–following (σ)/z–level) vertical coordinate (Bleck, 2002). Typically, the model includes isopycnal coordinates in the stratified ocean but uses the layered continuity equation to make a dynamically smooth transition to z–levels (fixed–depth coordinates) in the unstratified surface mixed layer or to σ–levels (terrain–following coordinates) in shallow water. The optimal coordinate is chosen every time step using a hybrid coordinate generator. In this way, the model automatically generates the lighter isopycnal layers needed for the pycnocline during summer, while the same layers may define z–levels during winter.

The model spans the entire globe north of $78.6°S$, with a Mercator grid from $66°S$ to $47°N$, at a resolution of $0.08° \cos(\text{lat}) \times 0.08°$ (latitude $\times$ longitude), and a bipolar Arctic patch north of 47°N, i.e., a tripole grid (Murray, 1996).

The average zonal (longitudinal) resolution for this 1/12.5° global grid varies from ≈ 9 km at the equator to ≈ 7 km at mid–latitudes (e.g., at 40°N) and ≈ 3.5 km at the north pole. The meridional (latitudinal) grid resolution is halved in the Antarctic for computational efficiency. The model's land–sea boundary is at the 10–m isobath and it potentially uses a terrain–following vertical coordinate in depths shallower than 140 m. The bottom topography was constructed from the NRL Digital Bathymetry Data Base (DBDB2) bathymetry data base, which has a resolution of 2–minutes and is available online at http://www7320.nrlssc.navy.mil/DBDB2_WWW/. Numerous hand-edits have been performed to improve coastlines and sill depths in key straits and passages.

There are 32 hybrid layers in the vertical in the model. The target density values for the isopycnals and the decreasing change in density with depth between isopycnal coordinate surfaces are based on the 1/4° Generalized Digital Environmental Model (GDEM) climatology (NAVOCEANO, 2003; Carnes, 2009). The density difference values were chosen, so that the layers tend to become thicker with increasing depth, with the lowest abyssal layer being the thickest. The minimum thickness of the top layer in deep water is 3 m, and this minimum increases 1.18$\times$ per layer up to a maximum of 450 m, and target densities are chosen such that at least the top four layers are always in z–level coordinates.

The initial model spin–up run was initialized from the January GDEM climatology and forced by years 1979–2002 from the European Centre for Medium–Range Weather Forecasts (ECMWF) 40–year Re–Analyses (ERA–40) (Kållberg et al, 2004) averaged to form a climatological monthly mean atmospheric forcing. The wind speeds were scaled to be consistent with QuikSCAT observations (Kara et. al., 2009). 6–hourly sub–monthly wind anomalies from the 0.5° Fleet Numerical Meteorology and Oceanography Center (FNMOC) Navy Operational Global Atmospheric Prediction System (NOGAPS; Rosmond et al. 2002) over year 2003 were added to the 12 monthly averages to obtain realistic mixed layer depths and to allow continuation with 3–hourly or 6–hourly interannual winds data sets.

5 Results

5.1 Description of runs and sampling issues

The results here are taken from four different simulations of HYCOM, designated by 9.7, 14.0, 14.1, and 14.2. HYCOM 9.7 serves as our control experiment, without any tidal forcing. It started from the end of the spin–up simulation and was run from 2003 through mid-2008 using 3-hourly Fleet Numerical Meteorology and Oceanography Center (FNMOC) Navy Operational Global Atmospheric Prediction System (NOGAPS) atmospheric forcing with wind speeds scaled to be consistent with QuikSCAT observations. HYCOM 14.0 was a test experiment, performed for just two months starting in July 2003 from HYCOM 9.7. HYCOM 14.0 included M_2 tidal forcing as well as wind- and buoyancy-forcing. Encouraged by the results of 14.0, we then proceeded to 14.1, an experiment again starting from 9.7 in July 2003 but covering 5 calendar years (2004 through 2008). HYCOM 14.1 included tidal forcing for M_2, S_2, N_2, and K_2 (the four largest semidiurnal constituents), and K_1, O_1, P_1, and Q_1 (the four largest diurnal constituents), as well as the same wind- and buoyancy-forcing used in 9.7.

At the vertical and horizontal resolutions utilized here, it is impractical to save full global three-dimensional output hourly for the full five years of the simulation. We did save daily 25-hour averages of three-dimensional 14.1 output. Since the 25-hour period is very close to twice that of the dominant tidal constituent M_2, most of the tidal motions are filtered out of these averages. For the full five-year duration of 14.1, we saved global hourly output of sea surface height, and other surface fields. We also saved hourly full three-dimensional output, over the last three years of the run, in a few domains of great interest for the study of internal tides, such as Hawai'i, the Indonesian Archipelago, and others. Finally, simulation 14.2 is a twin of 14.1 for May 2004 but saves full three-dimensional model output hourly, over the entire globe.

The combined size of the stored output of HYCOM 14.1 is 68 terabytes, and the single month in 14.2 accounts for another 3 TB. This is an enormous amount of material to analyze, and we have only begun to go through our results. Thus far a harmonic analysis of 14.1, commonly used to separate the contributions of the various tidal constituents, has been performed at only a limited number of locations, the 102 pelagic tide gauges of Shum et al. (1997). The harmonic analysis is used to determine the rms surface elevation errors of the eight constituents in 14.1 with respect to the tide gauge data. Harmonic analysis on every gridpoint in such a large model is a very time-consuming endeavor. For this reason, we defer some of the analyses we wish to pursue on 14.1 to later papers. In this paper, we will show 1) results from the harmonic analysis of 14.1 at the tide-gauge stations, 2) other results from 14.1 which do not require a time-consuming harmonic analysis, and 3) some results from harmonic analysis of M_2 in one day of output from experiment 14.0. These latter results are possible because 14.0 does not contain any other tidal constituents. However, they should be regarded as preliminary because the internal tide is not necessarily stationary, so that one day of output may not be sufficient for a rigorous analysis of the internal tides.

5.2 RMS surface elevation errors

Table 2 shows the time-averaged signals of the eight largest consituents averaged over the 102 pelagic tide gauges, the elevation errors of year 2004 from HYCOM 14.1 with respect to the tide gauge records of these eight constituents, and the percent of the tide gauge sea surface elevation variance of these constituents captured by the model. AGHS may be consulted for details on how such calculations are performed. We also analyzed years 2003 and 2006, and came up with virtually identical elevation errors. The overall percent variance captured, 92.6%, is very slightly lower than that captured in the optimally tuned two-layer simulations of AGHS, despite the higher horizontal resolution used here, which should improve the solutions (Egbert et al. 2004, Arbic et al. 2008). However, in the latter model the full spherical harmonic computation of SAL was utilized, whereas here we have used only the scalar approximation. We conclude that for our first attempt at a mixed wind-plus-tides simulation the errors are reasonably small. Based on the experience in the literature we believe these errors will reduce with a more rigorous treatment of SAL, and with the introduction of data assimilation.

5.3 Bottom speeds of non-tidal motions

Because our topographic wave drag scheme acts on bottom flows, and because the 25-hour filter we utilize along with the wave drag is an imperfect discriminator of tidal versus non-tidal flows, it is important to make sure that non-tidal bottom flows are not severely reduced with the addition of topographic wave drag. Figure 2a is a map of the mean kinetic energy 50 m above the bottom for HYCOM 9.7, averaged over 2006. Figure 2b displays the mean kinetic energy 50 m above the bottom for non-tidal flows in 14.1 (i.e. based on 25-hour filtered daily currents), also for 2006. The two figures were not computed in exactly the same way, since in Figure 2a the non-tidal flows (i.e. the total flows) were saved as daily snapshots whereas in Figure 2b the non-tidal flows were saved as 25-hour averages. However, as shown in Arbic et al. (2009), in present-day high-resolution models the non-tidal flows seem to be relatively unaffected by subsampling on scales of about a day. Comparison of the two figures, both of which mask out regions shallower than 1000 m, demonstrates that on the whole, adding the topographic wave drag to the model does not reduce the non-tidal bottom flow. Indeed, it appears that the non-tidal motions are on the contrary stronger in the tidally-forced case with topographic drag (14.1) than they are in the non-tidal case (9.7). We speculate that this may be because in the tidal run quadratic bottom boundary layer drag is effectively weaker than in the non-tidal case, in many locations. In the tidal case the resolved tidal velocity is often less (especially in the deep ocean) than the background 5 cm s^{-1} tidal flow commonly imposed in ocean general circulation models including in HYCOM 9.7. Another possibility is that some contribution from tidal flow is still present in the 25-hour averages from 14.1, which would tend to increase mean kinetic energy. However, a test of the eight-constituent AGHS run shows that this effect is likely to contribute a maximum of 7 cm^2 s^{-2} to the low-frequency kinetic energy in waters deeper than 1000 m. Some of the regions of large mean kinetic energy are also where the topographic wave drag is very strong (e.g. the Gulf of Mexico and some of the Indonesian Seas). Our 25-hour averaging scheme for applying this drag only to the tidal component appears to induce artificially large mean velocities in some locations. We are exploring alternative approaches for subsequent simulations with tides and eddies.

5.4 First-order impact of horizontally varying stratification

Figure 3a displays the amplitude of the M_2 internal tide signature in the steric sea surface height of HYCOM experiment 13.1, which is run under conditions like those in AGHS and SHA; with a horizontally uniform two-layer stratification, and no wind- and buoyancy-forcing. As in AGHS and SHA, large internal tide activity in the Drake passage is readily apparent, and is almost certainly artificially high, as noted by Padman et al. (2006). Large internal tide activity can also be seen in other polar regions e.g. the Labrador Sea and the Southern Ocean south of Africa. Figure 3b displays the same M_2 amplitude, but computed from one day of experiment 14.0; the wind, buoyancy-, and M_2-forced "warm-up" experiment. In this plot internal tide activity in the polar regions is much weaker, thus demonstrating a first-order effect of horizontally varying stratification on the internal tide field. In tropical and subtropical regions the internal tide activity is generally stronger in the wind-plus-tides simulation (Fig. 3b) than in the tide-only simulation (Fig. 3a).

5.5 Comparison of modeled internal tide to satellite altimeter data

We now compare the modeled sea surface signature of internal tides in the vicinity of Hawai'i to the signatures seen in along-track TOPEX/POSEIDON satellite altimeter data. The altimeter data was obtained by personal communication with Richard Ray in 2006, and is an updated version of the data reported on by Ray and Mitchum (1996, 1997). Figure 4 shows the altimeter tracks used in the comparison. The blue lines in Figure 5 show the M_2 elevation amplitudes and phases along track number 125, in observations and in HYCOM 14.0. The red lines denote the low-pass filtered (barotropic) versions of the signal. In Figure 6 we display the difference between the blue and red lines, i.e. the perturbations to the M_2 elevation amplitudes and phases at the sea surface due to internal tides. The modeled perturbations clearly have similar amplitude and horizontal length scale to the observations, but equally clearly do not match the observations "wiggle for wiggle" along the entire track length (some wiggles are matched fairly well, particularly in phase). In contrast, when high-resolution regional models forced at their horizontal boundaries by TOPEX/POSEIDON tidal amplitudes are compared to altimeter data (e.g. Carter et al. 2008 and references therein, among several), the comparison is better. The rms of the internal tide perturbations, averaged over all of the tracks shown in Figure 4 (using the latitude and longitude bounds shown in the Figure), are given in Table 3. Rms values are given for observations, AGHS, SHA, and HYCOM 14.0.[5] The rms of the differences between the observed and modeled

[5]Note that the amplitude perturbation values in Table 3 were incorrectly reported to be too low, by a factor of $\sqrt{2}$, in several seminars given by the first author.

perturbations (i.e. between the blue and red curves in Figure 6) are given in parentheses in Table 3. The AGHS internal tides are too weak, probably because of the relatively low 1/4° resolution used there, as evidenced by the low rms values compared to observations. The magnitudes of the SHA and HYCOM 14.0 pertubations are closer to those seen in observations, for both amplitude and phase. The poor "wiggle-for-wiggle" match of the models to observations is seen in the values of the rms differences between perturbations (the parenthetical values), which are nearly as large or larger than the rms values seen in the observations. Of the three global baroclinic tide simulations examined in this paper, HYCOM 14.0 yields the best combination of reasonably accurate barotropic tides combined with baroclinic tides that are at least of the correct magnitude. In future work we will examine the sea surface signal of internal tides, the temporal variability of this signal, and the comparison to satellite altimeter data, in much more detail, using a harmonic analysis of HYCOM experiment 14.1.

5.6 Co-existence of eddies and tides

We now show some figures which visually demonstrate the co-existence of tides and eddies in the HYCOM simulations. In Figure 7 we show a snapshot of the non-steric sea-surface height in the Pacific sector of HYCOM 14.1. The non-steric height is dominated by the large-scale barotropic tide. In Figure 8 we show snapshots over the same sector of the steric sea surface height. The first snapshot (Figure 8a) is taken at the same time as in Figure 7, while the second (Figure 8b), is taken six hours later. Western boundary currents, and mesoscale eddies, are easily discernible in Figure 8, as in many previous studies of high-resolution ocean models. Internal tides are visible as speckled patterns in several regions; for instance, in the central tropical Pacific. It is difficult by eye to discern differences in the patterns shown in Figures 8a and 8b. The differences between these two steric height fields are displayed in Figure 9. Even with a much smaller color scale, the meso- and gyre-scale general circulation features in Figures 8a and 8b are absent in the difference plot. Instead, we see the much higher frequency internal tides, which show up as beams as in Figure 3.

The co-existence of eddies and tides can be seen more easily in animations which we have submitted along with this paper. Hawaii.fli shows the steric and non-steric sea surface heights in a region around Hawai'i, for the last five days of June 2004. The non-steric field, dominated by the barotropic tide, evolves extremely rapidly, while in the steric field, the higher-frequency internal tide signals course rapidly through the geostrophic field, which appears to be at a standstill on these short timescales. Stericssh.gif, a movie of the steric sea surface height covering a much larger area as well as a longer time period, shows that internal tides are ubiquitous throughout the world ocean. Figure 10 shows the rms sea surface height variability over 2004 to 2007 from the two simulations (with 25-hour daily averaging in 14.1). These are remarkably similar, indicating that the appearance at least of the filtered near-surface eddy field is not significantly affected by tides.

Finally, we give some indication of the vertical structure of the simulation in Figures 11a and 11b. These figures, computed from experiment 14.1, display the zonal component of velocity (u) in the upper waters of a meridional section running through Hawai'i. Figure 11b shows the 25-hour mean while Figure 11a shows the snapshot at noon Zulu (UST). Layer interfaces are shown as solid black lines, and the thick black line is the mixed layer depth. The hybrid nature of HYCOM's vertical cooridinate is illustrated by the increasing number of near-surface layers that are flat (i.e. in z-coordinates) the further north in the plot. However, the majority of the layers are isopycnal and so give an indication of the density structure. There is much more structure in the "wiggles" of the interfaces between isopycnal layers in Figure 11a than in Figure 11b, indicating that many of the wiggles are from internal tides. These wiggles involve changes in vertical density structure and will have signatures in the steric sea surface height. Likewise, there is much more vertical structure in the velocity field in the snapshot than in the 25-hour average, indicating that the tides are a strong signal, and have significant vertical structure, in that field as well.

6 Summary and discussion of future work

In this paper we have shown some preliminary results of HYCOM simulations which simultaneously resolve barotropic tides, baroclinic tides, and an eddying general circulation. The nominal horizontal resolution of the simulation is $1/12.5°$, and there are 32 hybrid layers in the vertical direction. We have shown that a parameterized topographic wave drag can be inserted which yields a reasonably accurate sea surface elevation of the barotropic tide at the same time that the bottom flows of non-tidal motions are not severely reduced. The accuracy of the barotropic tide in the baroclinic simulations presented here is of comparable accuracy to that in the baroclinic simulations of Arbic et al. (2004–AGHS), and considerably more accurate than that in the main baroclinic simulation written about in Simmons et al. (2004–SHA).

The stratification in the simulation presented here can vary in the horizontal direction, since wind- and buoyancy forcing is present to support such variations. In contrast, the stratification in the earlier global baroclinic tide simulations of AGHS and SHA, which did not include wind- and buoyancy-forcing, was horizontally uniform. In both of those studies a typical midlatitude stratification was used throughout the entire globe, and internal tide activity in some polar regions (for instance, the Scotia Sea) was almost certainly artificially high (Padman et al. 2006). Comparison of the internal tide signature at the sea surface in HYCOM runs with a horizontally uniform stratification and tidal forcing only versus the more realistic horizontally varying stratification in a wind, buoyancy, and tidally forced run, indicates that internal tide activity in polar regions is much reduced in the latter compared to the former. Thus the allowance of a horizontally varying stratification with the inclusion of wind- and buoyancy-forcing has a first-order effect on the internal tide field.

Preliminary comparisons of the surface signature of the M_2 internal tide in the region around Hawai'i with satellite altimeter data indicate that the internal tides in HYCOM appear to have approximately correct magnitude. Similar comparisons show that the AGHS internal tides are too weak, while the SHA internal tides are of similar amplitude to the HYCOM internal tides. Tides in the HYCOM simulations presented here, unlike those in the AGHS and SHA simulations, appear to be reasonably accurate, by the measures described here, in both the barotropic and baroclinic fields. However, there is not in general a "wiggle-for-wiggle" match between the observations and the HYCOM model results. In a planned future paper we will investigate the surface signature of the internal tides, and their comparison to satellite altimeter data, in much more detail. This discussion is anticipated to be of value for the planned wide-swath satellite altimeter mission (Fu and Ferrari 2008), which will have to remove tides at small scales–i.e. on the scales of internal tides–if it is to succeed in its planned goal of studying geostrophic flows at sub-mesoscales. Comparison of the three-dimensional structure of tidal currents with current-meter data, detailed investigations of the interactions between tidal currents and the eddying general circulation, an investigation of the three-dimensional distribution of tidal mixing, and further investigations of the optimal method for introducing topographic wave drag into a mixed tidal/non-tidal simulation, are also underway based on the results of the simulations presented here.

7 Acknowledgements

This paper is dedicated to the memory of Peter Killworth, the founding editor of *Ocean Modelling* and an influential physical oceanographer. We thank Richard Ray for supplying us with the altimeter data on internal tides utilized in our Figures 4-6. This work is funded by the Office of Naval Research (ONR), as part of the National Ocean Partnership Program, under the project, U.S. GODAE: global ocean prediction with the HYbrid Coordinate Ocean Model (HYCOM). BKA acknowledges support from Naval Research Laboratory contract N000173-06-2-C003, and thanks Eric Chassignet and Harley Hurlburt for initiating this contract. EJM acknowledges support from ONR 6.1 project "Dynamics of the Indonesian Throughflow and its remote impact" under program element 61153N. HYCOM simulations were performed under the Department of Defense High Performance Computing Modernization Program an IBM SP POWER5+ at the Naval Oceanographic Office, Stennis Space Center, Mississippi and on a Cray XT4 at the United States Army Engineer Research and Development Center (ERDC), Vicksburg, MS. This is contribution NRL/JA/7320–09-9261 and has been approved for public release.

8 References

Arbic, B.K., Garner, S.T., Hallberg, R.W., Simmons, H.L, 2004. The accuracy of surface elevations in forward global barotropic and baroclinic tide models. Deep-Sea Res. II 51, 3069-3101.

Arbic, B.K., Mitrovica, J.X., MacAyeal, D.R., Milne, G.A., 2008. On the factors behind large Labrador Sea tides during the last glacial cycle and the potential implications for Heinrich events. Paleoceanography 23, PA3211, doi:10.1029/2007PA001573.

Arbic, B.K., Shriver, J.F., Hogan, P.J., Hurlburt, H.E., McClean, J.L., Metzger, E.J., Scott, R.B., Sen, A., Smedstad, O.M., Wallcraft, A.J., 2009. Estimates of bottom flows and bottom boundary layer dissipation of the oceanic general circulation from global high-resolution models. J. Geophys. Res. 114, C02024, doi:10.1029/2008JC005072.

Bell, T.H., 1975. Lee waves in stratified flows with simple harmonic time dependence. J. Fluid Mech. 67, 705-722.

Bleck, R. 2002. An oceanic general circulation model framed in hybrid isopycnic-cartesian coordinates. Ocean Modelling, 4, 55-88.

Carrere, L., Lyard, F., 2003. Modeling the barotropic response of the global ocean to atmospheric wind and pressure forcing–comparisons with observations. Geophys. Res. Lett. 30, 1275, doi:10.1029/2002GL016473.

Carnes, M.R., 2009. Description and evaluation of GDEM-V 3.0. Naval Research Laboratory report NRL/MR/7330–09-9165.

Carter, G.S., Merrifield, M.A., Luther, D.S., Becker, J.M., Katsumata, K., Gregg, M.C., Levine, M.D., Boyd, T.J., Firing, Y.L., 2008. Energetics of M_2 barotropic-to-baroclinic tidal conversion at the Hawai'ian Islands. J. Phys. Oceanogr. 38, 2205-2223.

Chassignet, E.P., Hurlburt, H.E., Smedstad, O.M., Halliwell, G.R., Hogan, P.J., Wallcraft, A.J., Baraille, R., Bleck, R., 2007. The HYCOM (HYbrid Coordinate Ocean Model) data assimilative system. J. Mar. Sys. 65, 60-83.

Chavanne, C., Flament, P., Zaron, E., Carter, G., Merrifield, M., Luther, D., Gurgel, K.-W., 2009a. The surface expression of semi-diurnal internal tides in the Kauai Channel, Hawai'i. Part I: observations and numerical predictions. Submitted to J. Phys. Oceanography.

Chavanne, C., Flament, P., Luther, D., Gurgel, K.-W., 2009b. The surface expression of semi-diurnal internal tides in the Kauai Channel, Hawai'i. Part II: Interactions with mesoscale currents. Submitted to J. Phys. Oceanography.

Egbert, G.D., Ray, R.D., 2000. Significant dissipation of tidal energy in the deep ocean inferred from satellite altimeter data. Nature 405, 775-778.

Egbert, G.D., Ray, R.D., 2003. Semi-diurnal and diurnal tidal dissipation from TOPEX/POSEIDON altimetry. Geophysical Research Letters 30, 1907 doi:10.1029/2003GL017676.

Egbert, G.D., Ray, R.D., Bills, B.G., 2004. Numerical modeling of the global semidiurnal tide in the present day and in the last glacial maximum. J. Geophys. Res. 109, C03003, doi:10.0129/2003JC001973.

Fu, L.-L., and R. Ferrari (2008), Observing oceanic submesoscales from space, Eos, 89 (48), 488.

Garner, S.T., 2005. A topographic drag closure built on an analytical base flux. J. Atmos. Sci. 62, 2302-2315.

Gill, A.E., 1982. Atmosphere-Ocean Dynamics. Academic Press, San Diego, 662 pp.

Griffiths, S.D., Peltier, W.R., 2008. Megatides in the Arctic Ocean under glacial conditions. Geophys. Res. Lett. 35, L08605, doi:10.1029/2008GL033263.

Griffiths, S.D., Peltier, W.R., 2009. Modelling of polar ocean tides at the Last Glacial Maximum: Amplification, sensitivity, and climatological implications. J. Climate, in press.

Hallberg, R., Rhines, P., 1996. Buoyancy-driven circulation in an ocean basin with isopycnals intersecting the sloping boundary. J. Phys. Oceanogr. 26, 913-940.

Hendershott, M.C., 1972. The effects of solid earth deformation on global ocean tides. Geophysical Journal of the Royal Astronomical Society 29, 389-402.

Hibiya, T., Nagasawa, M., Niwa, Y., 2006. Global mapping of diapycnal diffusivity in the deep ocean based on the results of expendable current profiler (XCP) surveys. Geophys. Res. Lett. 33, L03611, doi:10.1029/2005GL025218.

Jayne, S.R., St. Laurent, L.C., 2001. Parameterizing tidal dissipation over rough topography. Geophys. Res. Lett. 28, 811-814.

Kållberg, P., A. Simmons, S. Uppala, and M. Fuentes, 2004. ERA-40 Project Report Series, the ERA–40 archive. 17, 31 pp, U.K.

Kara, A. B., A. J. Wallcraft, P. J. Martin, and R. L. Pauley, 2009. Optimizing surface winds using QuikSCAT measurements in the Mediterranean Sea during 2000-2006. J. Mar. Syst., doi:10.1016/j.jmarsys.2009.01.020.

Lee, M.-M., Nurser, A.J.G., Coward, A.C., de Cuevas, B.A., 2007. Eddy advective and diffusive transports of heat and salt in the Southern Ocean. J. Phys. Oceanogr. 37, 1376-1393.

Lyard, F., Lefevre, F., Letellier, T., Francis, O., 2006. Modelling the global ocean tides: Modern insights from FES2004. Ocean Dynamics 56, 394-415, doi:10.1007/s10236-

006-0086-x.

Maltrud, M.E., McClean, J.L., 2005. An eddy resolving global 1/10° simulation. Ocean Modelling 8, 31-54.

Marshall, D.P., Naveira-Garabato, A.C., 2008. A conjecture on the role of bottom-enhanced diapycnal mixing in the parameterization of geostrophic eddies. J. Phys. Oceanogr. 38, 1607-1613.

Masumoto, Y., Sasaki, H., Kagimoto, T., Komori, N., Ishida, A., Sasai, Y., Miyama, T., Motoi, T., Mitsudera, H., Takahashi, K., Sakuma, H., Yamagata, T., 2004. A fifty-year eddy-resolving simulation of the World Ocean–Preliminary outcomes of OfES (OGCM for the Earth Simulator). J. Earth Simulator 1, 35-56.

Murray, R. J. 1996. Explicit generation of orthogonal grids for ocean models, J. Comp. Phys., 126, 251–273.

Naveira-Garabato, A.C., Polzin, K.L., King, B.A., Heywood, K.J, Visbeck, M., 2004. Widespread intense turbulent mixing in the Southern Ocean. Science 303, 210-213.

NAVOCEANO, 2003. Database description for the generalized digital environmental model (GDEM-V) Version 3.0, OAML–DBD–72, 34 pp, Stennis Space Center, MS.

Nikurashin, M., 2008. Radiation and dissipation of internal waves generated by geostrophic motions impinging on small-scale topography. PhD thesis, Masssachusetts Institute of Technology/Woods Hole Oceanographic Institution Joint Program.

Padman, L., Howard, S., Muench, R., 2006. Internal tide generation along the South Scotia Ridge. Deep-Sea Res. II 53, 157-171, doi:10.1016/j.dsr2.2005.07.011.

Polzin, K.L., Toole, J.M., Ledwell, J.R., Schmitt, R.W., 1997. Spatial variability of turbulent mixing in the abyssal ocean. Science 276, 93-96.

Park, J.-H., Watts, D.R., 2006. Internal tides in the Southwestern Japan/East Sea. J. Phys. Oceanogr. 36, 22-34.

Rainville, L., Pinkel, R., 2006. Propagation of low-mode internal waves through the ocean. J. Phys. Oceanogr. 36, 1220-1237.

Ray, R.D., 1998. Ocean self-attraction and loading in numerical tidal models. Marine Geodesy 21, 181-192.

Ray, R.D., 1999. A global ocean tide model from TOPEX/POSEIDON altimetry: GOT99.2, National Aeronautics and Space Administration Technical Memorandum, NASA/TM-1999-209478, 58 pp.

Ray, R.D., Mitchum, G.T., 1996. Surface manifestation of internal tides generated near Hawai'i. Geophysical Reseach Letters 23, 2101-2104.

Ray, R.D., Mitchum, G.T., 1997. Surface manifestation of internal tides in the deep ocean: Observations from altimetry and tide gauges. Progress in Oceanography 40, 135-162.

Rosmond, T.E., Teixeira, J., Peng, M., Hogan, T.F., Pauley, R., 2002. Navy Operational Global Atmospheric Prediction System (NOGAPS): Forcing for Ocean Models. Oceanography 15, 99-108.

Schiller, A., Fiedler, R., 2007. Explicit tidal forcing in an ocean general circulation model. Geophys. Res. Lett. 34, L03611, doi:10.1029/2006GL028363.

Shriver, J.F., Hurlburt, H.E., Smedstad, O.M., Wallcraft, A.J., Rhodes, R.C., 2007. 1/32° real-time global ocean prediction and value-added over 1/16° resolution. J. Marine Systems 65, 3-26.

Shum, C.K., Woodworth, P.L., Andersen, O.B., Egbert, G.D., Francis, O., King, C., Klosko, S.M., Le Provost, C., Li, X., Molines, J.-M., Parke, M.E., Ray, R.D., Schlax, M.G., Stammer, D., Tierney, C.C., Vincent, P., Wunsch, C.I., 1997. Accuracy assessment of recent ocean tide models. J. Geophys. Res. 102, 25173-25194.

Simmons, H.L., Hallberg, R.W., Arbic, B.K., 2004. Internal wave generation in a global baroclinic tide model. Deep-Sea Res. II 51, 3043-3068.

Simmons, H.L., 2008. Spectral modification and geographic redistribution of the semi-diurnal internal tide. Ocean Modelling 21, 126-138, doi:10.1016/j.ocemod.2008.01.002.

Smith, W.H.F., Sandwell, D.T., 1997. Global sea floor topography from satellite altimetry and ship depth soundings. Science 277, 1956-1962.

Uehara, K., Scourse, J.D., Horsburgh, K.J., Lambeck, K., Purcell, A.P. 2006. Tidal evolution of the northwest European shelf seas from the Last Glacial Maximum to the present. J. Geophys. Res. 111, C09025, doi:10.1029/2006JC003531.

Willebrand, W., Barnier, B., Boning, C., Dieterich, C., Killworth, P.D., Le Provost, C., Jia, Y., Molines, J.-M., New, A.L., 2001. Circulation characteristics in three eddy-permitting models of the North Atlantic. Progr. Oceanogr. 48, 123-161, doi:10.1016/S0079-6611(01)00003-9.

Zaron, E., Chavanne, C., Egbert, G., Flament, P., 2009. Baroclinic tidal generation in the Kauai Channel inferred from high-frequency radio Doppler current meters. Dynamics of Atmospheres and Oceans, in press.

Table 1: Energies and elevation errors of barotropic part of earlier forward global baroclinic tide models, compared to results from an altimetry-constrained tide model. Globally integrated surface available potential energy (APE) and barotropic kinetic energy (KE) of M_2 are computed from (1) Table 1 of Egbert and Ray (2003–ER2003 below–based on an altimetry-constrained barotropic model), (2) main baroclinic simulation of AGHS (see their Figure 11), (3) AGHS simulation without parameterized topographic wave drag and with only a scalar approximation for self-attraction and loading (SAL); i.e. conditions like those in the main simulation of SHA, (4) main SHA simulation (see their Figure 8), (5) a simulation in the appendix of SHA, with an artificially large c_d value of 0.3 standing in as a proxy for topographic wave drag. Units of energies are 10^{17} J. Globally averaged sea-surface elevation discrepancies (cm) with respect to GOT99, computed over latitudes equatorward of 66° and waters deeper than 1000 m, are also given. Numbers in parantheses indicate percent of open-ocean sea surface elevation variance captured.

Model	Surface APE	Barotropic KE	RMS elevation discrepancy
ER2003	1.34	1.78	–
AGHS main baroclinic simulation	1.48	1.73	7.37 (92.4)
AGHS, no parameterized drag, scalar SAL	3.18	3.46	17.14 (58.8)
SHA main baroclinic simulation	4.37	5.09	23.35 (23.5)
SHA, large c_d as proxy for wave drag	1.66	2.03	9.88 (86.3)

Table 2: Time and station-averaged sea-surface height signals at the set of 102 pelagic tide gauges used in Shum et al. (1997), and sea-surface elevation errors of year 2004 of our HYCOM multi-constituent foward simulation with respect to the gauges. Numbers in parantheses denote percentage of sea-surface height variance at the gauges captured by HYCOM.

Constituent	Signal (cm)	HYCOM error (cm)
Q_1	1.62	0.68 (82.1)
O_1	7.76	2.48 (89.7)
P_1	3.62	0.79 (95.2)
K_1	11.26	2.48 (95.1)
N_2	6.86	1.40 (95.9)
M_2	33.22	8.26 (93.8)
S_2	12.62	5.17 (83.2)
K_2	3.43	1.65 (76.9)
RSS	39.04	10.63 (92.6)

Table 3: Rms of the internal tide perturbations to M_2 sea surface elevation amplitudes and phases, computed across all of the tracks shown in Figure 4, from altimetric observations, AGHS, SHA, and HYCOM 14.0. Rms values of the difference in perturbations (model minus observations) are given in parantheses

Source	RMS amplitude perturbation (cm)	RMS phase perturbation (degrees)
Observations	0.87	4.35
AGHS	0.40 (0.86)	1.91 (3.93)
SHA	1.07 (1.29)	4.66 (5.64)
HYCOM 14.0	1.03 (1.15)	4.42 (4.58)

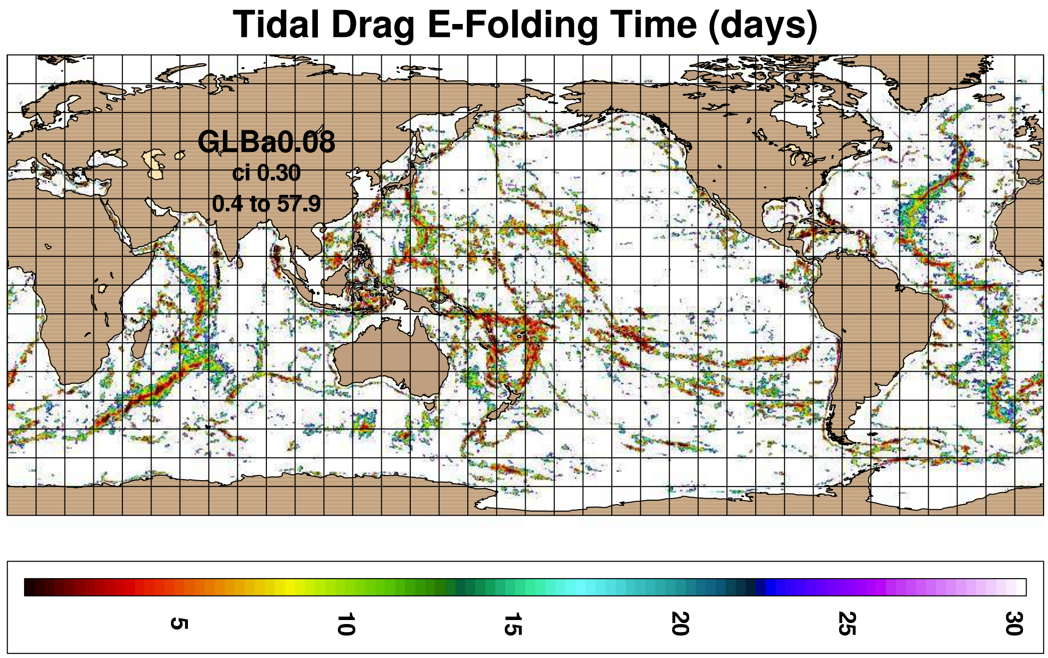

Figure 1: e-folding time (days) for topographic wave drag with drgscl=1. The majority of the white areas have no wave drag at all.

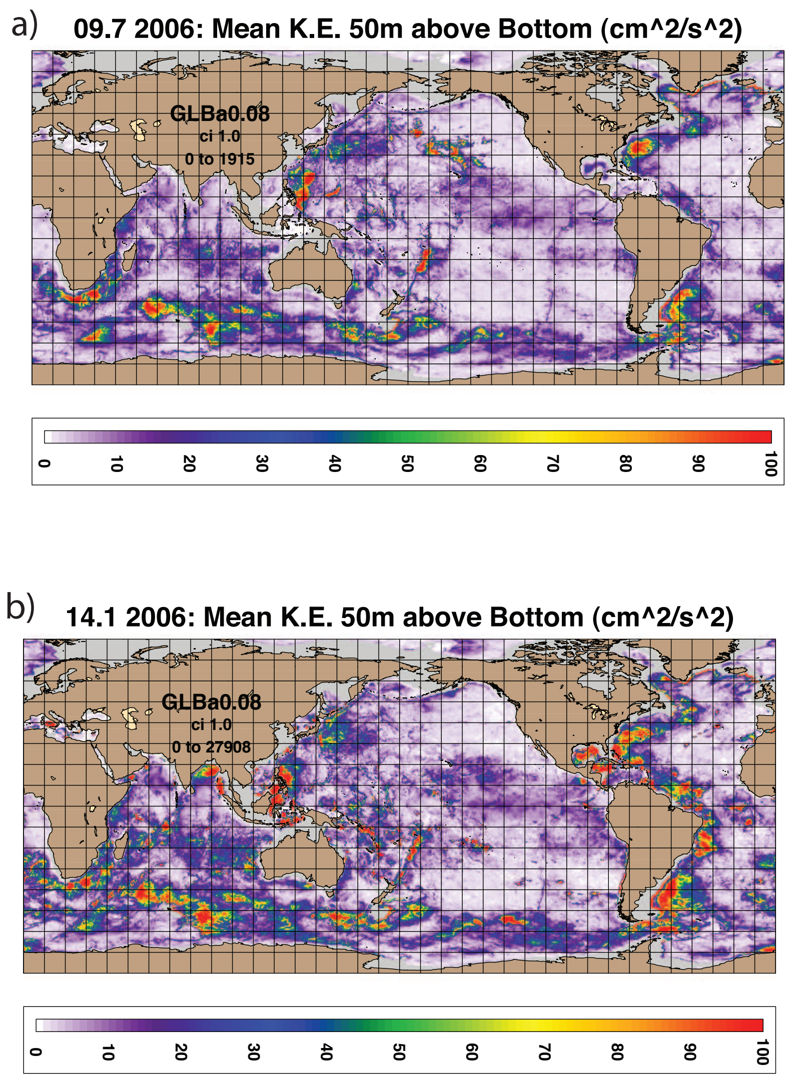

Figure 2: Annual mean kinetic energy (cm^2/s^2) 50 m above the bottom from (a) daily snapshots from 2006 in HYCOM experiment 9.7, which does not have tidal forcing, (b) daily 25-hour averages from 2006 in HYCOM experiment 14.1, in which forcing of the eight largest tidal constituents is included. The 25-hour averages filter out most of the tidal component of the near bottom velocities. Regions shallower than 1000 m are in grey.

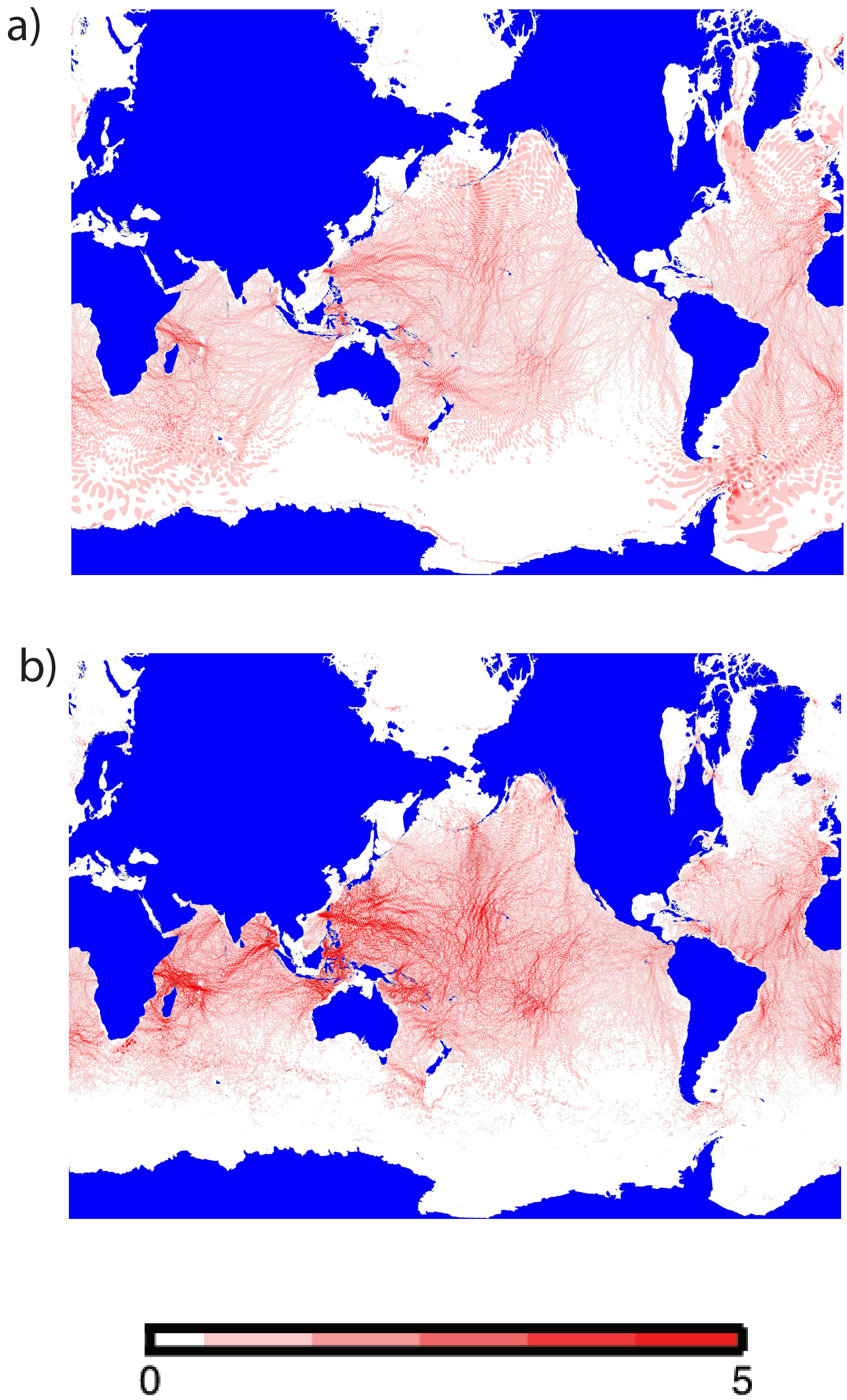

Figure 3: Amplitude (cm) of M_2 internal tide signature in steric ssh of HYCOM experiment (a) 13.1 (two-layer, horizontally uniform stratification, M_2 forcing only), (b) 14.0 (short warm-up run for 14.1; 32-layer, horizontally non-uniform stratification, wind-, buoyancy-, and M_2-forcing included.)

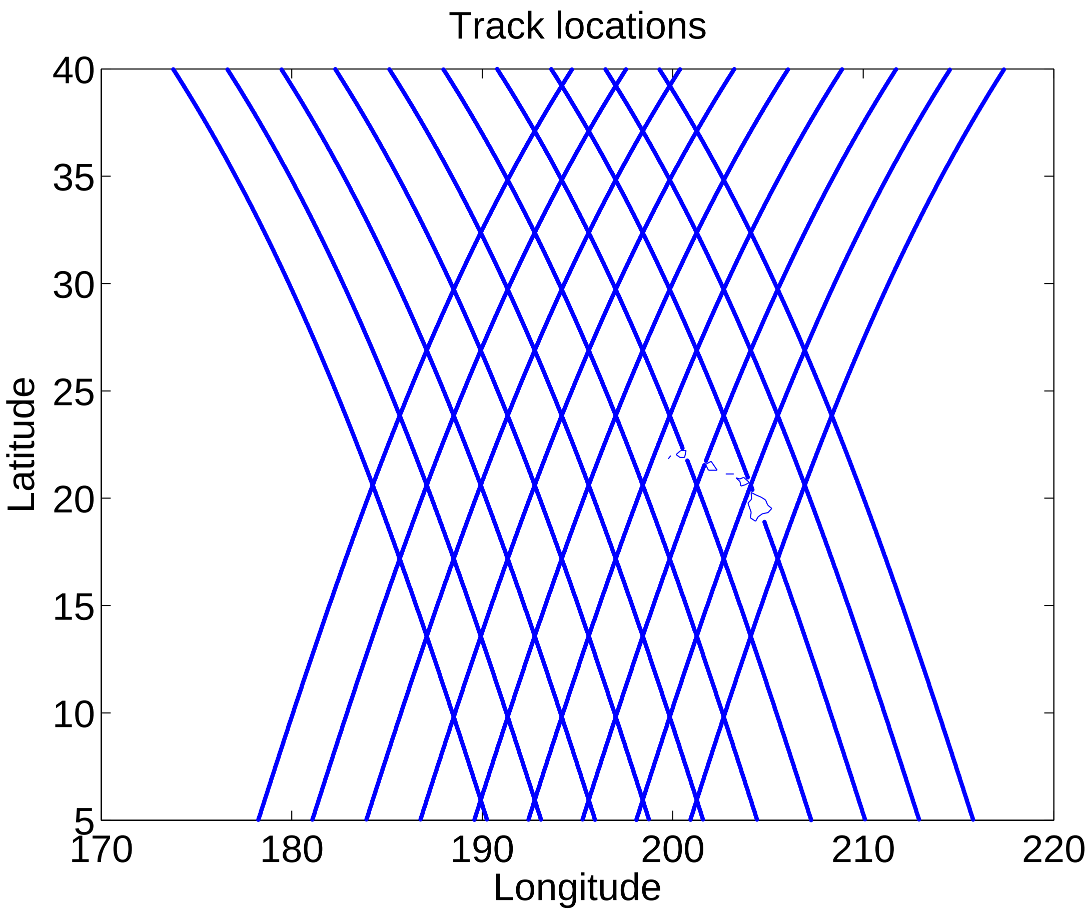

Figure 4: TOPEX/POSEIDON tracks for which altimetric data (around Hawai'i) on surface signature of M_2 internal tides is utilized here.

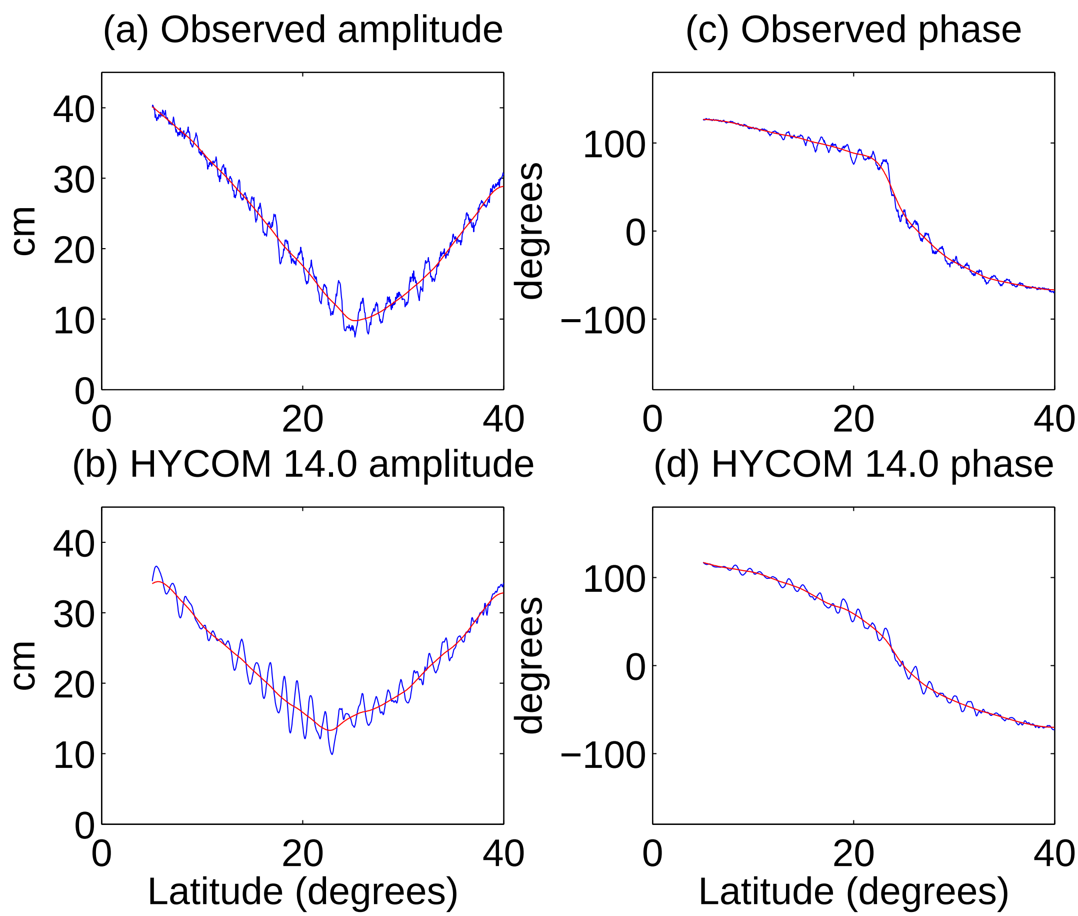

Figure 5: Amplitudes (a, observed and b, HYCOM 14.0) and phases (c, observed and d, HYCOM 14.0) of the M_2 internal tide signature in sea surface elevation along altimetric track number 125. HYCOM 14.0 is a 32-layer, wind-, buoyancy-, and M_2- forced simulation. Blue lines represent full signal (barotropic plus baroclinic), red lines represent low-pass filtered (barotropic) signal.

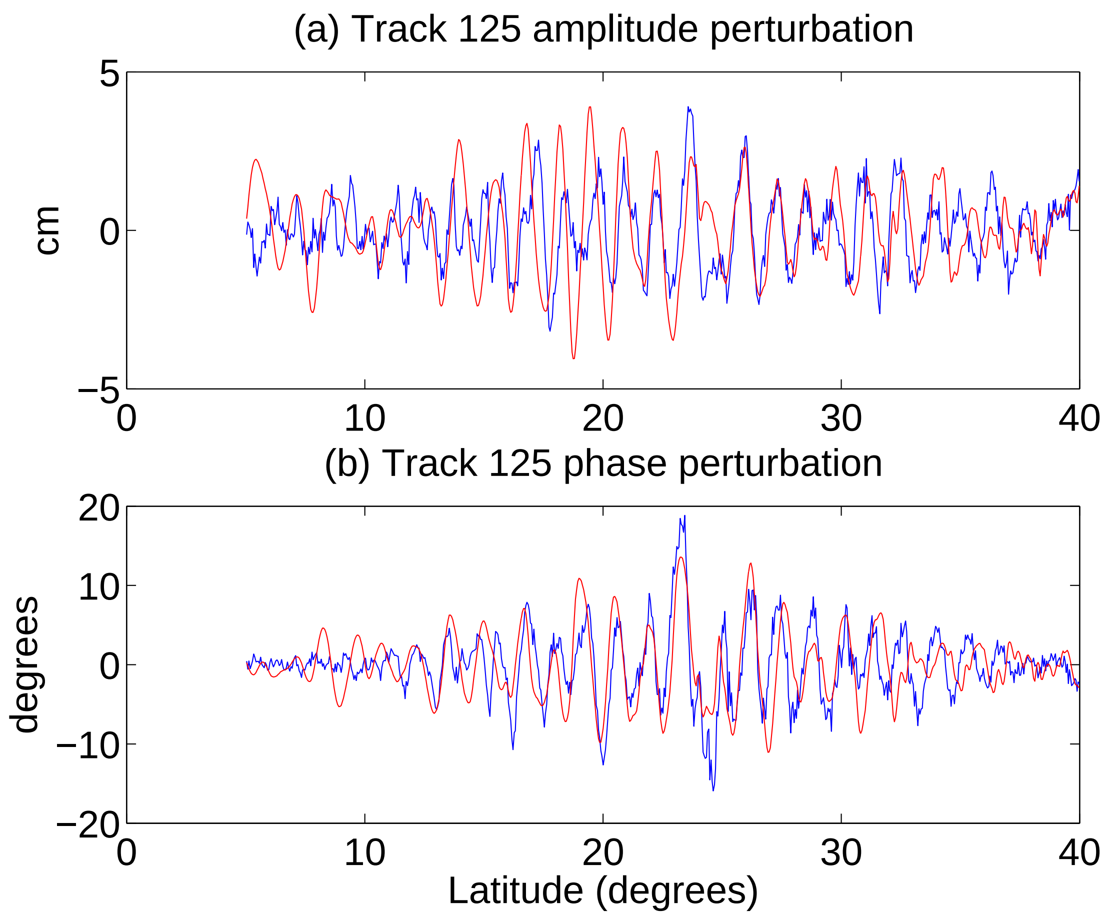

Figure 6: Internal tide perturbations to (a) amplitude and (b) phase of M_2 sea surface elevation along altimetric track 125. Altimetric observations are in blue, while HYCOM 14.0 is in red.

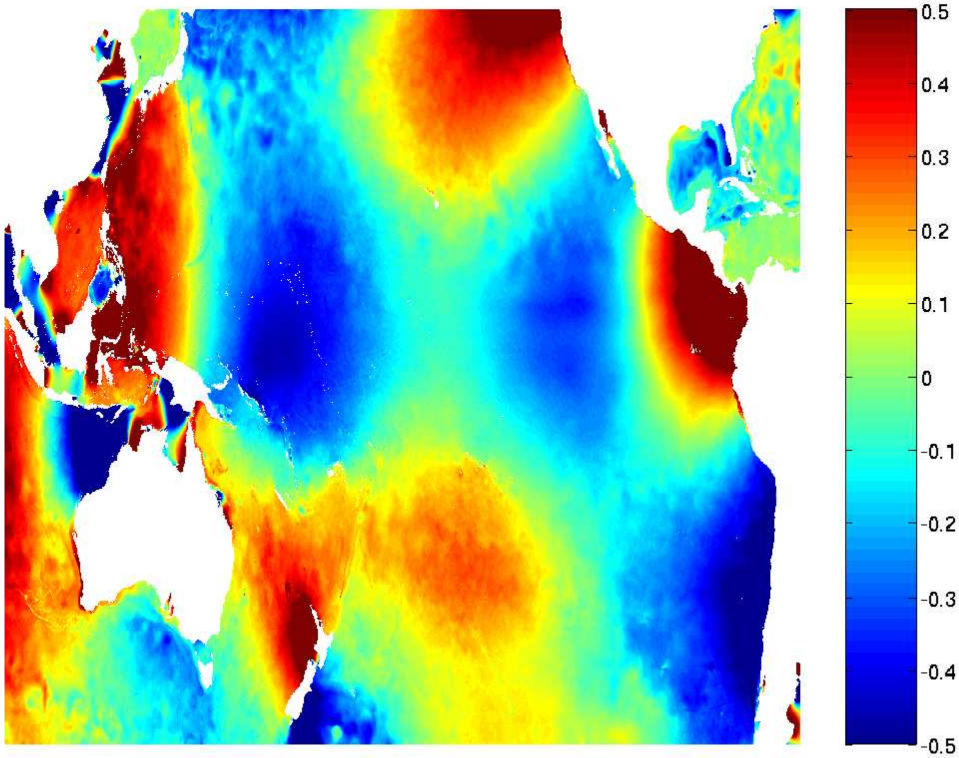

Figure 7: Pacific portion of global snapshot of non-steric sea surface height (m) on June 30, 2006 at 00Z.

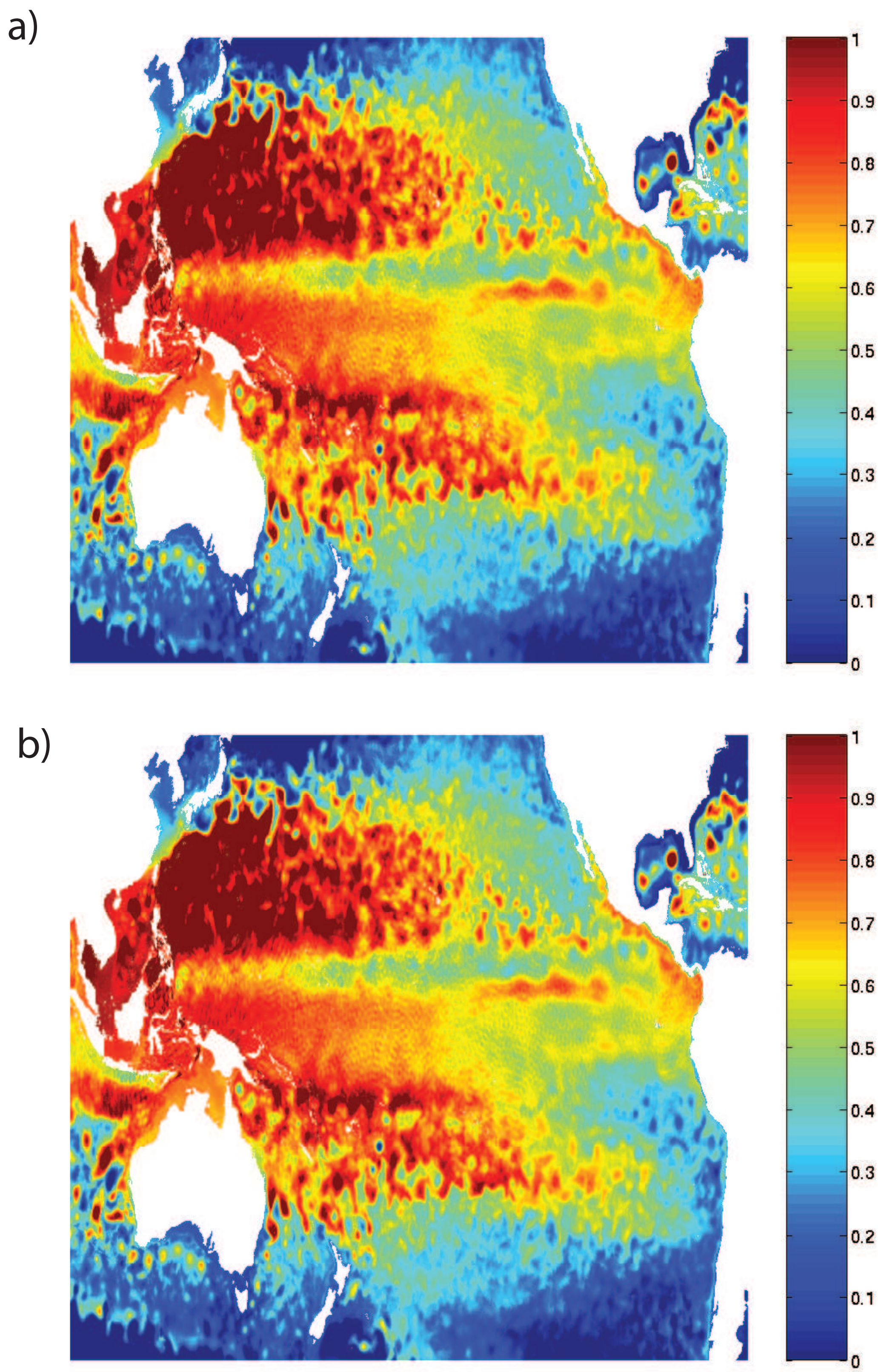

Figure 8: Pacific portion of global snapshot of steric sea surface height (m) on June 30, 2006 at (a) 00Z and (b) 06Z.

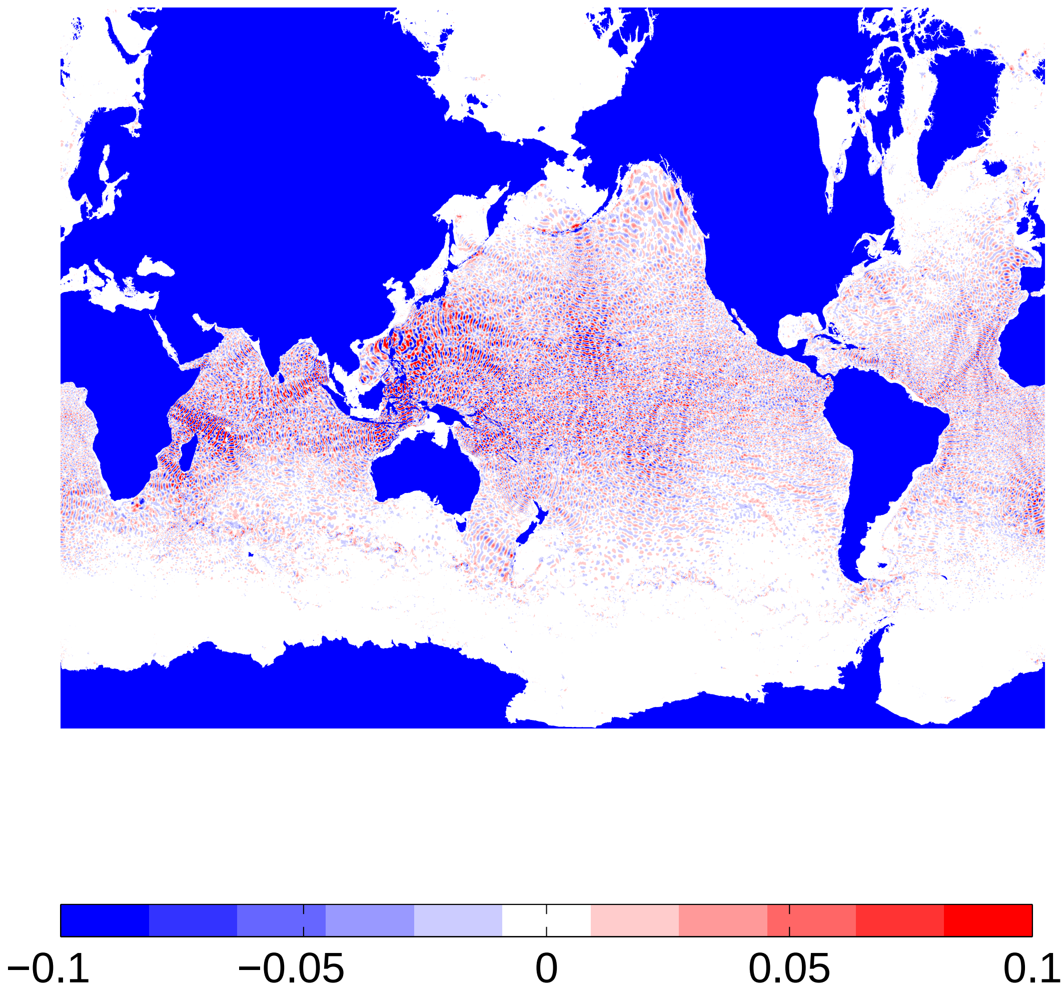

Figure 9: Global difference in steric sea surface heights (m) from snapshots taken 6 hours apart; June 30, 2006, 06Z-00Z.

a)

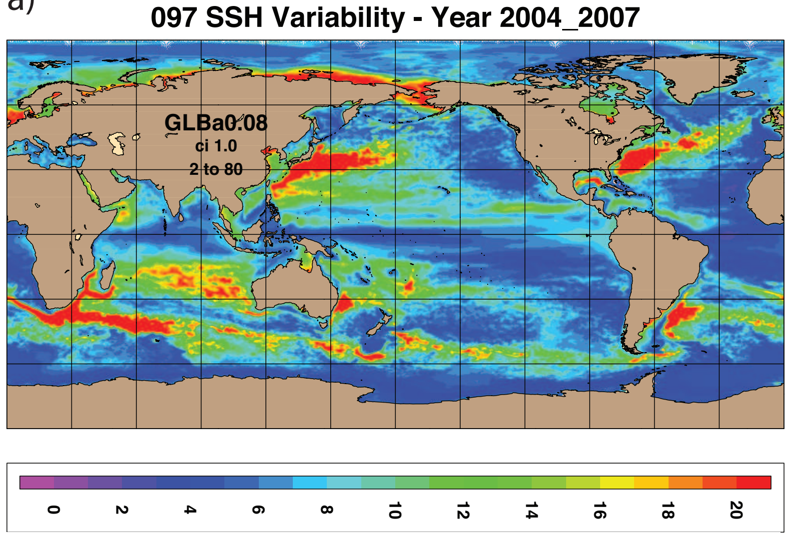

b)

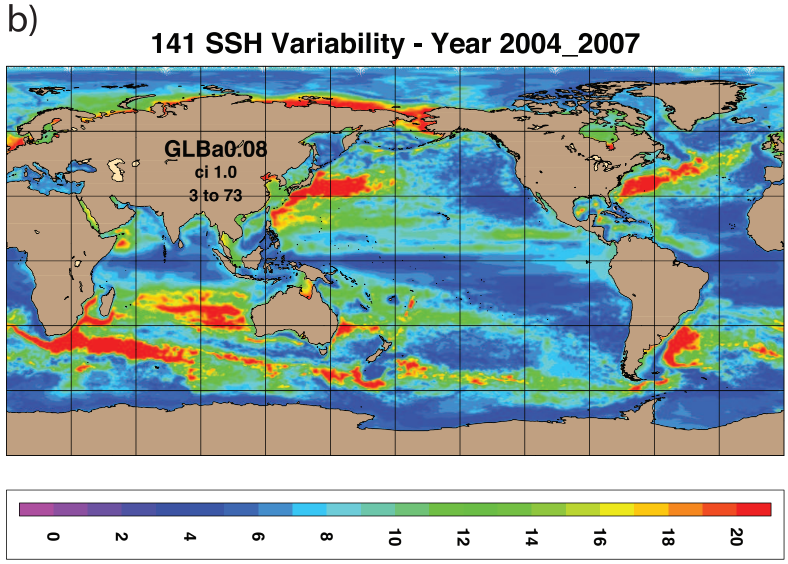

Figure 10: 2004-2007 root mean square (RMS) sea surface height (SSH) variability (cm) from (a) HYCOM 9.7 (no tides) and (b) HYCOM 14.1 (with tides; mean computed from daily 25-hour averages).

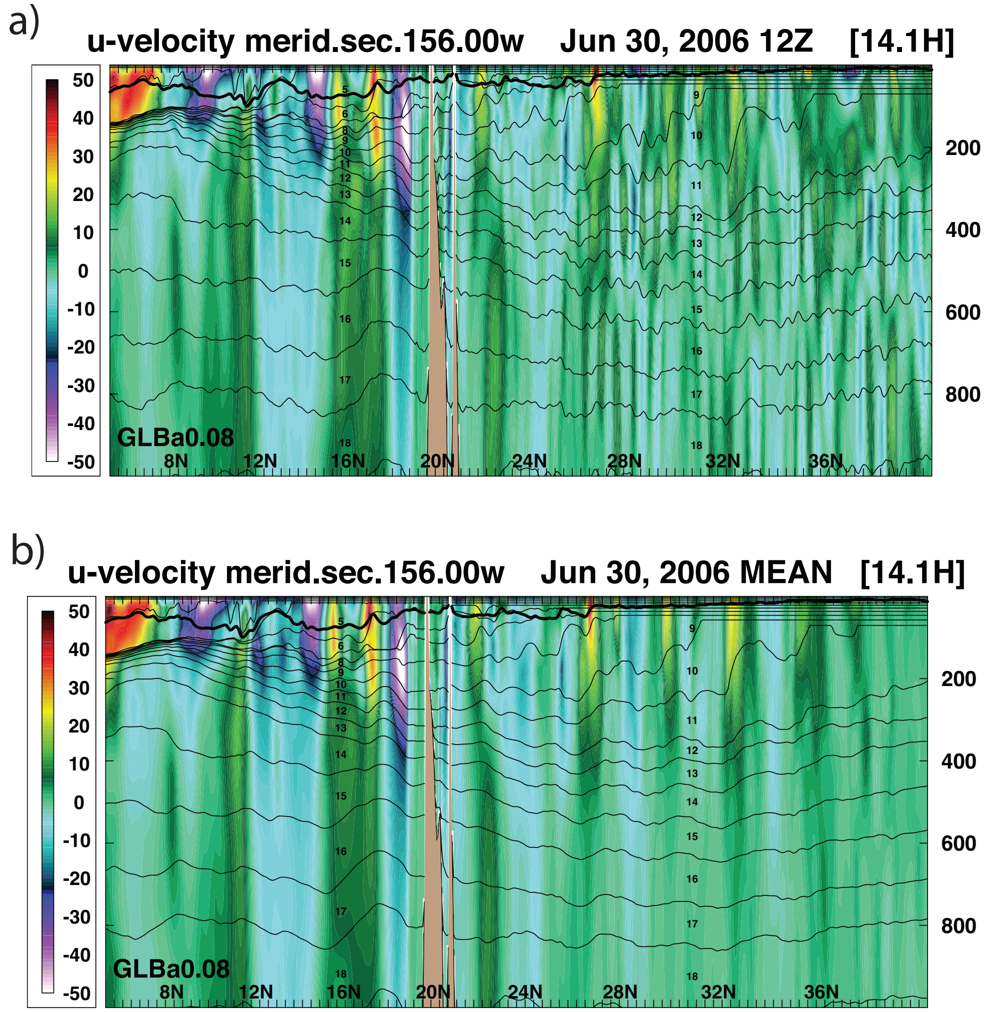

Figure 11: u-velocity (cm s^{-1}) in 156°W section through Hawai'i on June 30, 2006; (a) snapshot and (b) 25-hour mean. Isopycnal locations (black lines) shown versus depth in meters (right axes).